



HAL
open science

A new numerical framework for the full field modeling of dynamic recrystallization in a CPFEM context

D.A. Ruiz Sarrazola, D. Pino Muñoz, Marc Bernacki

► To cite this version:

D.A. Ruiz Sarrazola, D. Pino Muñoz, Marc Bernacki. A new numerical framework for the full field modeling of dynamic recrystallization in a CPFEM context. *Computational Materials Science*, 2020, 179, pp.109645. 10.1016/j.commatsci.2020.109645 . hal-03191628

HAL Id: hal-03191628

<https://hal.science/hal-03191628>

Submitted on 22 Aug 2022

HAL is a multi-disciplinary open access archive for the deposit and dissemination of scientific research documents, whether they are published or not. The documents may come from teaching and research institutions in France or abroad, or from public or private research centers.

L'archive ouverte pluridisciplinaire **HAL**, est destinée au dépôt et à la diffusion de documents scientifiques de niveau recherche, publiés ou non, émanant des établissements d'enseignement et de recherche français ou étrangers, des laboratoires publics ou privés.



Distributed under a Creative Commons Attribution - NonCommercial 4.0 International License

A new numerical framework for the full field modeling of dynamic recrystallization in a CPFEM context

D. A. Ruiz Sarrazola^{a,*}, D. Pino Muñoz^a, M. Bernacki^a

^a*MINES ParisTech, PSL - Research University, CEMEF - Centre de mise en forme des matériaux, CNRS UMR 7635, CS 10207 rue Claude Daunesse, Sophia Antipolis Cedex 06904, France.*

Abstract

This work describes the coupling of a level-set (LS) based numerical framework for microstructural evolutions modeling with a crystal plasticity finite elements method (CPFEM), in order to propose a new full field approach dedicated to dynamic recrystallization (DRX) modeling. These developments are proposed for 3D polycrystalline metals subjected to large deformations at high temperatures.

CPFEM is one of the best available alternatives to model the evolution of dislocation densities, and misorientation during plastic deformation. The dislocation density and misorientation is then used as input data for the recrystallization model. Grain boundary migration (GBM) is modeled by using a kinetic law which links the velocity of the grain boundaries, described by LS functions, with the thermodynamic driving pressures. The nucleation of new grains is modeled by using phenomenological laws, which define the number of nucleation sites as a function of the dislocation density and the misorientation. The link between the CPFEM and the GBM model gives an accurate description of the DRX phenomenon, which is intended to model industrial processes.

In this work the methods and the coupling algorithm are presented, along with an analysis of the different numerical parameters and strategies to define nucleation. The calibration and validation of the model against experimental

*Corresponding author

Email addresses: david-alejandro.ruiz_sarrazola@mines-paristech.fr (D. A. Ruiz Sarrazola), daniel.pino_munoz@mines-paristech.fr (D. Pino Muñoz), marc.bernacki@mines-paristech.fr (M. Bernacki)

Preprint submitted to Computational Materials Science

March 6, 2020

data for 304L steel will be presented in a future work.

Keywords: Dynamic recrystallization, Crystal plasticity, Level-set, FEM, Full field model

Acronyms

- LS - Level-set.
- CP - Crystal plasticity
- CPFEM -crystal plasticity finite element method.
- DRX - Dynamic recrystallization.
- DDRX - Discontinuous dynamic recrystallization.
- CDRX - Continuous dynamic recrystallization.
- GBM - Grain boundary migration.
- FEM - Finite element method.
- FFT - Fast Fourier transformation.
- CPFFT - Crystal plasticity fast Fourier transformation.
- RSS - Resolved shear stress.
- CRSS - Critical resolved shear stress.
- MP - Material point.

1. Introduction

Current industrial processes require the production of metallic materials with high mechanical properties. To improve the mechanical properties, it is necessary to control the evolution of the microstructure during thermo-mechanical processing.

During thermo-mechanical processing the microstructure evolves due to the interaction of several phenomena: plastic deformation causes the generation and accumulation of dislocations, the accumulation of dislocations causes grains to rotate, and because of the high temperatures, dislocations

are able to move and annihilate causing dynamic recovery. The accumulation of dislocations also leads to the formation of low angle grain substructures which can evolve into high angle grain boundaries leading to the formation of new grains with low dislocations densities (nucleation). Simultaneously the dislocations density gradients between grains (which translate into accumulated energy gradients) combined with capillarity effects, cause GBM. The interaction of these phenomena constitutes the DRX mechanism [1].

DRX is the main microstructure evolution process, which determines the final state of the material microstructure after thermo-mechanical processing. Depending on the scale at which new nuclei can be identified, the DRX process is classified as discontinuous (DDRX) or continuous (CDRX) [2].

For materials with low to medium stacking fault energy like 304L steel, that are the initial focus of this work. The recrystallization process is generally considered as DDRX [2].

The need to control the microstructure has led to development of numerous models for dynamic recrystallization [2, 3]:

- Phenomenological models, like the JMAK type models, which describe the evolution of the global recrystallization fraction and mean grain size as a function of the strain and temperature [4, 5, 6], these models only describe average behaviors by fitting phenomenological laws to experimental data.
- Mean field models, which describe the state of the microstructure as the average of a n-number of grains. The evolution of each grain follows phenomenological laws, that compare the state of each grain against the average state of the microstructure [7, 8, 9, 10, 11, 12]. Mean field models do not include and can not describe grains topology and interactions between neighbouring grains.
- Full field models which describe the microstructure topology at the polycrystal scale and allow to consider local phenomena and interactions between neighbouring grains. Several types of full field models exist in the literature:
 - Probabilistic models like the Monte-carlo and cellular automata models. These models use uniform grids formed by cells in order to describe the microstructure and use stochastic laws in order to model the evolution of the microstructural state [13, 14, 15, 16, 17, 18].

- Deterministic approaches, rely on the resolution of partial differential equations to describe the evolution of the microstructure. Deterministic methods can be divided according to their representation of the grain boundary network between front tracking and front capturing numerical frameworks.
- Front tracking methods like the vertex approach, explicitly describe the grains interfaces by using vertices, and models their evolution by computing the velocity of set of points [19, 20]. Front tracking methods can present limitations when dealing with appearance and disappearance of new grains, especially in 3D.
- On the other hand front capturing approaches like the level-set [21, 22, 23, 24, 25, 26] and phase field [27, 28, 29, 30, 31, 32] method circumvent this problem by describing the grains interface implicitly with auxiliary functions (distance functions or phase functions). Some comparisons have been performed between two methods, for GBM modeling, showing that in terms of accuracy both approaches have similar performance [33]. Main limitation of these approaches remains generally their complexity and numerical cost.

Both FEM and Fast Fourier transformation (FFT) [23, 34] methods have been coupled with the LS method. Even-tough FFT is largely more computational efficient than FEM, its requirements for structured mesh excludes its use for very large deformation cases that remeshing operations and to undergo complex shape evolutions. The recent improvements in terms of computational cost [35, 36] make the LS-FEM approach a powerful numerical framework to model dynamic recrystallization in the context of industrial applications.

The existing LS-FEM approach to model DDRX [10, 25] focuses on the description of GBM and nucleation, simplifying the plastic deformation. This results in a limited description of the processes involved in dynamic recrystallization. Also since both GBM and nucleation depend on the dislocation density, whose evolution during dynamic recrystallization is lead by plastic deformation. The ability to correctly model the local evolution of the microstructure thanks to this approach is limited.

To circumvent this limitation it is necessary to propose a more accurate description of the plastic deformation phenomena. Given the anisotropic behavior of plastic deformation and the scale of interest, the best alternative are

crystal plasticity (CP) formulations [37, 38, 39, 40]. CP describes precisely plastic deformation mechanisms at the microstructure level.

Models that combine classic recrystallization models with CP formulations have been proposed in the literature: mean field recrystallization models have been coupled with viscous-plastic self consistent CP models [9, 41, 42, 43], taking advantage that both models represent the microstructure as a n-number of grains. Probabilistic full field models have been coupled with both CPFEM and CPFFT simulations [44, 45, 46, 47]. In the case of deterministic models the phase field method has been coupled with CPFFT simulations [48, 49, 50]. However these models do not provide an appropriate framework to perform 3D full field simulations of dynamic recrystallization in context of industrial processes, where high plastic deformation can be achieved.

In this context, a 3D full field LS approach, coupled with a CPFEM, to model DDRX in context of large deformations is proposed. The CPFEM follows a Lagrangian framework, which combined with remeshing operations, allows to model large deformation. In the first section of this work the CPFEM framework is introduced, followed by the description of the LS approach for grains representation, grain boundary kinetics, and the formulation to model nucleation. Then global scheme coupling the models is described. Finally the models numerical parameters are analyzed along with different nucleation schemes.

2. Formulation

In this section, first the CPFEM framework to model plastic deformation is presented, along with the constitutive equations. Then the LS formulation to represent the microstructure and GBM is presented, and finally the phenomenological model that describes nucleation occurrence, is detailed.

The CPFEM is based on the variational solution of the momentum equilibrium equation by using the weak form of the principle of virtual work in a finite volume element. In CPFEM, the stress - strain response of each element is defined by a single crystal model. The specific details of the FEM method have already been described in the literature, and will not be presented in this work. The interested reader can refer to [51, 52, 53], here only the single crystal model will be further detailed.

The single crystal follows an elasto-viscoplastic formulation, following the work of Marin [54]. In order to model large plastic deformation a Lagrangian

framework is used, the nodes positions are updated after each iteration, further details can be found in [55, 56].

The single crystal model formulation follows the decomposition of the deformation gradient tensor \mathbf{F} , into an elastic part \mathbf{F}_e and a plastic part \mathbf{F}_p . The elastic deformation gradient is further decomposed into the left elastic stretch tensor \mathbf{V}_e and the elastic rotation tensor \mathbf{R}_e .

$$\mathbf{F} = \mathbf{F}_e \mathbf{F}_p = \mathbf{V}_e \mathbf{R}_e \mathbf{F}_p . \quad (1)$$

The plastic deformation gradient takes the body from the initial configuration B_0 , to the intermediate configuration \tilde{B} , lattice orientation does not change. The elastic rotation takes the body to an additional intermediate configuration $\tilde{\tilde{B}}$, the lattice orientation changes. Finally the elastic stretch takes the body to the final configuration B .

Considering that the elastic strains are orders of magnitude lower than the plastic strains, the infinitesimal strain assumption is introduced.

$$\mathbf{V}_e = \mathbf{1} + \boldsymbol{\epsilon}_e \quad \|\boldsymbol{\epsilon}_e\| \ll 1 , \quad (2)$$

with $\boldsymbol{\epsilon}_e$ the infinitesimal elastic deformation tensor. In this context the kinematics of the single CP model are defined by the stretch rate tensor \mathbf{d} and the spin rate tensor \mathbf{w} , defined as:

$$\mathbf{d} = \dot{\boldsymbol{\epsilon}}_e + \boldsymbol{\epsilon}_e \boldsymbol{\Omega}_e - \boldsymbol{\Omega}_e \boldsymbol{\epsilon}_e + \mathbf{d}_p , \quad (3)$$

$$\mathbf{w} = -skew(\dot{\boldsymbol{\epsilon}}_e \boldsymbol{\epsilon}_e) + \boldsymbol{\Omega}_e + \mathbf{w}_p , \quad (4)$$

with $\boldsymbol{\Omega}_e = \dot{\mathbf{R}}_e \mathbf{R}_e^T$ denoted as the spin of the lattice, \mathbf{d}_p the plastic strain rate and \mathbf{w}_p the plastic spin rate.

For a tensor \mathbf{A} , the *skew* operation is defined as $skew(\mathbf{A}) = 0.5(\mathbf{A} - \mathbf{A}^T)$ and the *sym* operation is defined as $sym(\mathbf{A}) = 0.5(\mathbf{A} + \mathbf{A}^T)$.

Considering that crystallographic slip is the main deformation mechanism, \mathbf{d}_p and \mathbf{w}_p are calculated as the summation of the slip rates $\dot{\gamma}^\alpha$, over all the slip systems α as :

$$\mathbf{d}_p = \sum_{\alpha=1}^n \dot{\gamma}^\alpha sym(\tilde{\mathbf{Z}}^\alpha) , \quad (5)$$

$$\mathbf{w}_p = \sum_{\alpha=1}^n \dot{\gamma}^\alpha \text{skew} \left(\tilde{\mathbf{Z}}^\alpha \right) , \quad (6)$$

with $\tilde{\mathbf{Z}}^\alpha$ the Schmidt tensor aligned to lattice current orientation defined as

$$\tilde{\mathbf{Z}}^\alpha = \tilde{\mathbf{s}}^\alpha \otimes \tilde{\mathbf{m}}^\alpha , \quad (7)$$

with \otimes denoting the dyadic product, $\tilde{\mathbf{s}}^\alpha = \mathbf{R}_e \mathbf{s}^\alpha$ the rotated vector in the slip plane direction, and $\tilde{\mathbf{m}}^\alpha = \mathbf{R}_e \mathbf{m}^\alpha$ the rotated vector normal to the slip plane.

The slip rates magnitude $\dot{\gamma}^\alpha$ are defined by the flow rule as a function of the the resolved shear stress (RSS) τ^α , and the critical resolved shear stress (CRSS) k^α , defined by the hardening law. The flow rule and hardening rule are presented in the next section. τ^α acting on a slip system is defined as:

$$\tau^\alpha = \boldsymbol{\tau} : \text{sym} \left(\tilde{\mathbf{Z}}^\alpha \right) , \quad (8)$$

with $\boldsymbol{\tau} = \det(1 + \boldsymbol{\epsilon}_e) \boldsymbol{\sigma}$ the Kirchhoff stress, Where $\boldsymbol{\sigma}$ is the Cauchy stress. The Kirchhoff stress is defined by the constitutive law as:

$$\boldsymbol{\tau} = \tilde{\mathcal{C}} : \boldsymbol{\epsilon}_e , \quad (9)$$

with $\tilde{\mathcal{C}}$ the elasticity tensor, rotated to the lattice current orientation. The values of $\tilde{\mathcal{C}}$ are material dependent, for the case of 304L steel isotropic elasticity is considered, so $\tilde{\mathcal{C}}$ can be defined by the young module (E) and the Poisson's ratio (ν).

2.1. Flow rule and hardening rule

The described framework is compatible with several flow rules and hardening rules found in literature [38]. The ones used in this work follows previous characterization performed on the material of interest 304L austenitic steel, which has a face centered cubic (FCC) crystal structure [10, 57].

The flow rule used, is a traditional power law defined as:

$$\dot{\gamma}^\alpha = \dot{\gamma}_0^\alpha \left(\frac{|\tau^\alpha|}{k^\alpha} \right)^{1/m} \text{sign}(\tau^\alpha) , \quad (10)$$

with $\dot{\gamma}_0^\alpha$ the reference slip rate and m the slip rate sensitivity coefficient both considered as material parameters. For a non nul scalar b the *sign*

operation is defined as $sign(b) = |b|/b$. The hardening follows the Joshie-Laasraoui-Jonas (YLJ) equation [58]. For FCC crystals it remains to consider only 1 CRSS for all the slip systems [54, 10, 57], so the CRSS $k^\alpha = k$ is defined as:

$$k^\alpha = k = k_0 + \psi \mu b \sqrt{\rho} , \quad (11)$$

with $k_0 = \sigma_0/M$ the initial microscopic yield stress of the material, σ_0 the macroscopic yield stress of the material, ψ a material dependent parameter, b the burger's vector magnitude, M the Taylor factor, and ρ the dislocation density, which evolves following:

$$\dot{\rho} = \left(\frac{K_1}{M} - \frac{K_2}{M} \rho \right) \sum_{\alpha=1}^n |\dot{\gamma}^\alpha| , \quad (12)$$

with K_1 and K_2 material parameters related to the generation of dislocations and the dynamic recovery respectively.

2.2. Grain representation

In this framework a grain is described thanks to a LS function ψ defined over a domain Ω , as the signed distance to the boundary Γ . The values of ψ are evaluated at each FE node (P1 interpolation). The adopted convention considers $\psi > 0$ inside the grain and $\psi < 0$ outside the grain [21, 22, 59].

$$\psi(x, t) = \pm d(x, \Gamma(t)) , \forall x \in \Omega , \quad (13)$$

$$\Gamma(t) = \{x \in \Omega, \psi(x) = 0\} , \quad (14)$$

with d the minimum euclidean distance from the point x to the interface Γ . At the start of the simulation the initial microstructure is generated by using a Voronoi tessellation or a Laguerre-Voronoi tessellation [60]. The microstructure is immersed in a unstructured FE mesh as LS functions as shown in figure 1.

From the initial microstructure the initial grain properties are generated. A random orientation is given to each grain, all nodes that belong to the grain have the same initial orientation. Similarly an initial dislocation density value constant per grain is assigned to each FE node.

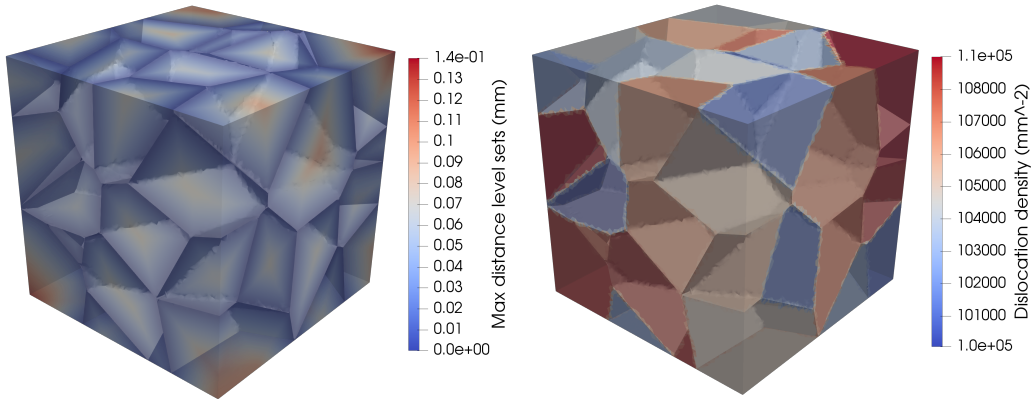


Figure 1: Max value of LS functions (left side) and initial dislocation density constant per grain (right side) in an unstructured finite element mesh representing 3D microstructure generated using Voronoi tessellation. Contours show the 0 value of the level set functions, i.e. the grain boundary network.

However since the CP calculations are performed over the elements, the orientation and dislocations fields defined over the nodes (P1 fields), must be transformed into fields defined over the elements (P0 fields).

For elements with all nodes belonging to the same grain the value assigned to the element corresponds to the value of the grain. For elements with nodes belonging to different grains, the orientation value that represents the minimal rotation with respect to the reference frame is assigned to the element (This definition constitutes a first approach, other definitions might be used). For the dislocation density a weighted average is performed between the dislocation values of the grains that the nodes belong to, with the weights being the volume of the element belonging to each grain.

2.3. Grain boundary migration (GBM)

As mentioned in the introduction, at high temperature the grains boundaries will evolve due to capillarity effects and energy gradients across grain boundaries. In the LS framework used in this work the kinematics of the grain boundary are calculated by solving a transport equation using FEM, for a given velocity \mathbf{v} field:

$$\frac{\partial \psi(x, t)}{\partial t} + \mathbf{v} \cdot \nabla \psi(x, t) = 0, \quad (15)$$

with ∇ the gradient operator. The velocity field is calculated by considering capillarity \mathbf{v}_c effects and energy gradients \mathbf{v}_e effects defined as:

$$\mathbf{v} = \mathbf{v}_c + \mathbf{v}_e , \quad (16)$$

$$\mathbf{v}_c = -M_b \gamma_b \Delta \psi \nabla \psi , \quad (17)$$

$$\mathbf{v}_e = M_b [|E_0|] \nabla \psi , \quad (18)$$

$$M_b = M_0 \exp \left(\frac{-Q_m}{RT} \right) , \quad (19)$$

with M_b the grain boundary mobility calculated according to the Arrhenius law, M_0 the mobility pre-exponential factor, material dependent, Q_m the activation energy for grain boundary migration, material dependent, R the universal gas constant, T the absolute temperature (K), $\Delta \psi$ the laplacian of ψ equivalent trace of the curvature tensor, γ_b the grain boundary energy which in this framework is considered isotropic (material dependent), and $[|E_0|]$ the jump of the stored energy due to dislocations accumulation across the grain boundary.

The stored energy is calculated as:

$$E_v = d_e * \rho , \quad (20)$$

with d_e being the dislocation line energy defined as a material dependent property.

This calculation framework has already been validated and optimized, with coloring techniques that include more than one grain per level set function, reducing the computational cost of the calculation. Further details can be found in [21, 22, 25, 59].

To calculate the energy field that will be used in the velocity calculation, first the P0 dislocation density field resulting from the CP calculation is transformed into a P1 field. This dislocation density field is an heterogeneous field, even inside the grains. This would result in a highly heterogeneous velocity field.

In other to correctly solve the transport equation with a highly heterogeneous velocity field a very refined mesh can be used, but it increases dramatically the computational cost of the whole simulation [61]. To reduce the

computational cost the dislocation density field is averaged per grain in order to calculate the transport velocity as shown in figure 2

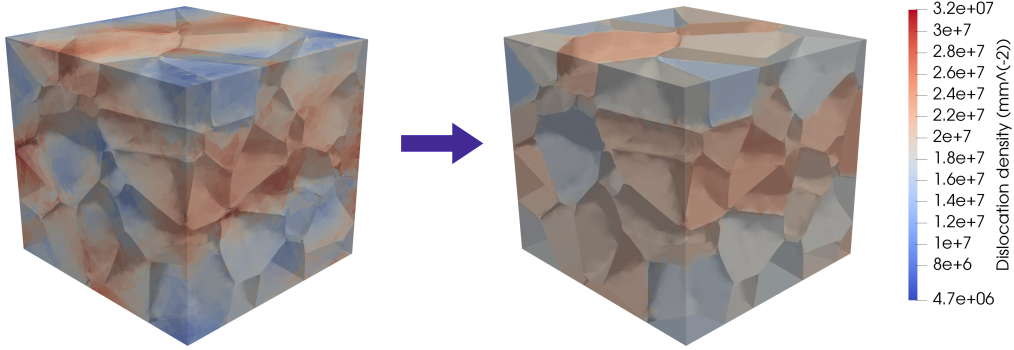


Figure 2: P0 dislocation density field from CP calculation (left side) and its corresponding averaged per grain P1 dislocation density field for the calculation GBM velocity (right side).

GBM is driven by a reduction of the stored energy, which implies a decrease of the dislocation density field inside the grains. Swept areas are assigned a minimal or annealed dislocation density ρ_0 which is material dependent. To take into account this effect into the CP calculation the P0 dislocation density field must be updated. This is done in the finite elements by considering:

$$\rho_e = \rho_{e\ t-dt} (1 - f_{swept}) + \rho_0 (f_{swept}) , \quad (21)$$

with ρ_e the dislocation density in the element after the GBM, $\rho_{e\ t-dt}$ the dislocation density in the element before GBM, and f_{swept} the swept volume fraction of the element.

2.4. Nucleation

Nucleation is modeled by coupling phenomenological laws with the LS framework, this approach has been previously used in the literature to model both dynamic and static recrystallization [10, 25, 59]. In this work it is further adapted to work in a CP framework.

Since the nucleated grains have a low dislocation density, they are introduced in the model with a ρ_0 dislocation density value. The different considerations for nucleation are described next:

2.4.1. Critical dislocation density

The critical dislocation density ρ_{cr} , defines when and where nucleation can occur, is calculated in an iterative way, following eq. 22.

$$\rho_{cr} = \left[\frac{-2\gamma_b \dot{\epsilon} \frac{K_2}{M_b d_e^2}}{\ln \left(1 - \frac{K_2}{K_1 \rho_{cr}} \right)} \right]^{1/2}, \quad (22)$$

Eq. 22 is derived from the critical dislocation density equation introduced by **Roberts and Ahlblom** [62], where some of the parameters were renamed in order to ensure compatibility with the current framework.

2.4.2. Nucleus Size

A nucleus radius r^* is calculated according to the **Bailey-Hirsch** criterion, eq. 23. This criteria approximates the condition that the stored energy is high enough to overcome the capillarity forces, and that the nucleus will not disappear.

This criteria is based on the assumption of perfect spherical grains. It requires a mesh size small enough to correctly describe the nuclei topology. Therefore a numerical safety factor ω is introduced, to compensate for errors in the description of the nucleus topology.

$$r^* = \omega \frac{2\gamma_b}{\rho_{cr} d_e} \quad (23)$$

2.4.3. Nucleus location

Classical nucleation models use the following criteria to define nucleation sites: first, nucleus can only appear in positions with an average dislocation density higher than the previously defined critical dislocation density. This combined with the nucleus size defined by eq. 23 ensures that the nucleus will grow. Second, it is initially assumed that nucleus can only appear near the grain boundaries, this is done by defining a distance d from the grain boundary which is equal to the nucleus diameter $2r^*$. The appearance of nucleus near the boundaries ensures the presence of misorientation, and is in accordance to necklace nucleation. However different criteria considering dislocation density gradients, misorientation, and misorientation gradients can also be defined. In section 4.5 different criteria and their impact on the simulation results are analyzed.

2.4.4. Nucleation Rate

The number of nuclei that are going to be introduced is represented as a volume of nuclei per unit of time \dot{V} , calculated with a variation of the proportional model of **Peczak and Luton** [63]:

$$\dot{V} = k_g \phi dt , \quad (24)$$

with k_g a probability coefficient that depends of the strain rate and temperature, and ϕ the total area or volume of the elements with dislocation density higher than the critical value, depending on the type of nucleation considered (necklace or bulk).

2.4.5. Post Nucleation

After a nucleus is introduced the P0 dislocation density and orientation fields must be updated in order to reflect the nucleation effect in the CP calculations. It is done in the following way: for the dislocation density field, as mentioned before the nucleated grains will have a dislocation density equal to the minimal dislocation density ρ_0 . The update procedure for the elements in which a nucleus appears follows the one used for the GBM. The new dislocation field is calculated as:

$$\rho_e = \rho_{e-t-dt} (1 - f_{nuc}) + \rho_0 (f_{nuc}) \quad (25)$$

With f_{nuc} the volume fraction of the element occupied by the nucleus.

For the orientation field, the nucleus orientation will be the orientation of the parent grain (grain in which the center of the nucleus is located) plus a random misorientation of minimum 15 degrees. This criteria is defined as a first approach, but further analyses with experimental data must be performed as there is no clear definition for the nucleus orientation. For the elements orientation field, only the elements with all their nodes inside the nucleus are affected. The same orientation is assigned to all the elements.

The difference in the selection of affected elements, causes that some elements near the nuclei boundaries will only have their dislocation density field updated. However the orientations field can not be treated in the same way as the dislocation density field.

Figure 3 illustrates the update of the dislocation density field after nucleation.

Updating the dislocation density fields and orientation fields, creates additional localized gradients and breaks the equilibrium state of the CPFEM

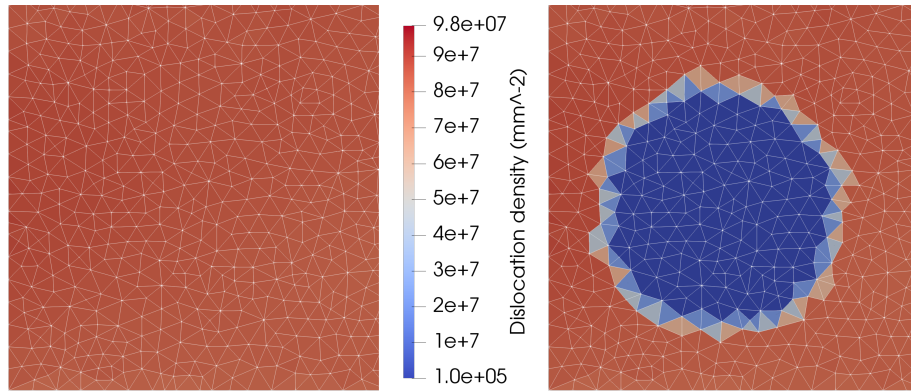


Figure 3: 2D view of the elements affected by the introduction of the nucleus: dislocation density field.

calculation. This can affect the convergence of the next CPFEM calculation. The strategy used in order to ensure the convergence of the CPFEM calculation will be presented in section 4.

3. Model Coupling

The coupling of the models requires several considerations in order to reach an optimal solution in terms of numerical cost, convergence and accuracy:

- The CPFEM calculation requires a smaller time step for its resolution, than the GBM calculation.
- In order to ensure convergence and minimize the computational cost of the CPFEM calculation, the time step needs to be adapted during the simulation. This is further detailed in section 4.
- The element quality deteriorates with each iteration as the node positions are updated after each CPFEM iteration. Therefore remeshing operations must be performed to ensure a good mesh quality.
- GBM calculations require several operations making them more computationally costly than CPFEM calculations.
- Use of very small time steps in the GBM calculations can lead to numerical errors. This is further detailed in section 4.

- The insertion of nuclei requires that the mesh size is small enough to correctly describe the nuclei topology. Since nuclei have a smaller size than the rest of the original microstructure, the mesh must be refined before nuclei are inserted.
- As the dislocation density increases because of the plastic deformation, the nucleus size defined by eq. 23 decreases. Therefore the mesh size must be refined during deformation.
- Remeshing operations in 3D have a very high computational cost.
- The time step required for nuclei to be inserted at each iteration is higher than the time required for CPFEM calculations.

Taking the previous consideration into account. The implemented coupling algorithm utilizes two different time steps (For constant strain rate it is equivalent to a deformation step), one for the CPFEM iterations and one for the GBM iterations. Additionally the remeshing and nucleation operations are only performed when the GBM iteration is performed.

For a clearer description the coupling algorithm is summarized in figure 4.

3.1. Reference simulation

The presented coupling algorithm allows to perform full field 3D simulations of dynamic recrystallization. The simulations provide information of the average state of the microstructure and also describe the local evolution of the microstructure, including interactions between neighbours.

Figure 5 shows an example simulation of the compression of a domain composed of 400 initial grains. The simulation was ran on 4 processors of 24 cores each. The simulation time is shown to illustrate, as the computational cost is the main limitation of the presented numerical framework. Also see animation 1.

The evolution of the microstructure during this work is described in terms of: recrystallized fraction X (eq. 26), volume-weighted mean grain size \bar{R} (eq.27), volume-weighted recrystallized mean grain size eq. 28 and number of grains.

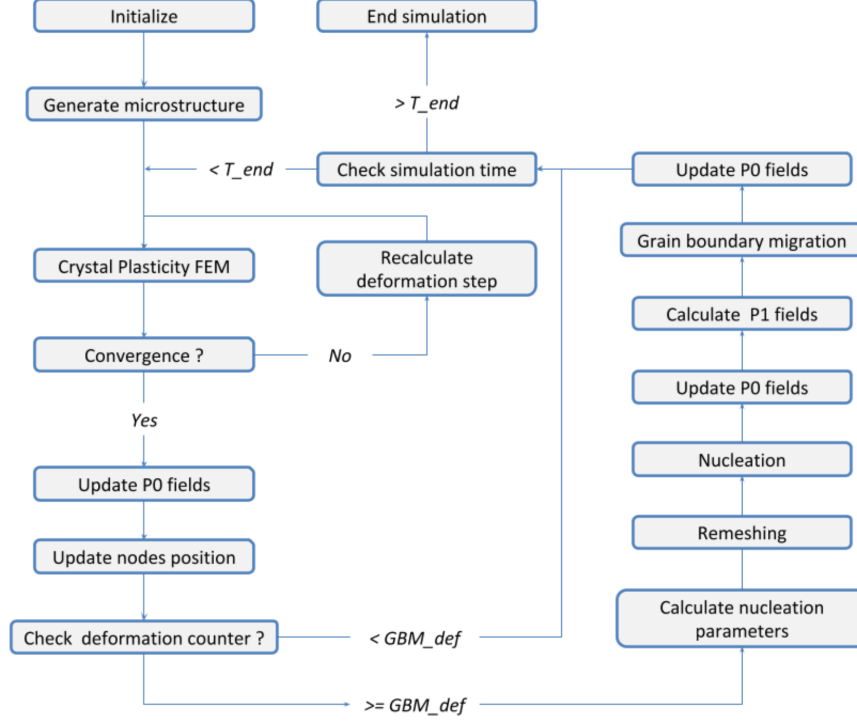


Figure 4: Coupling algorithm between the CPFEM and the dynamic recrystallization model.

$$X = \frac{\sum_{i=1}^{n_{Rx}} S r_i}{S_T} \quad (26)$$

with n_{Rx} the number of recrystallized grains, S_i the volume of the corresponding grain, and S_T the total volume of the domain.

$$\bar{R} = \frac{\sum_{i=1}^n r_i S_i}{S_T} \quad (27)$$

with n the total number of grains and r_i the equivalent spherical radius of each grain.

$$\bar{R}_X = \frac{\sum_{i=1}^{n_{Rx}} r_i S_i}{S_X}, \quad (28)$$

with S_X the total recrystallized volume.

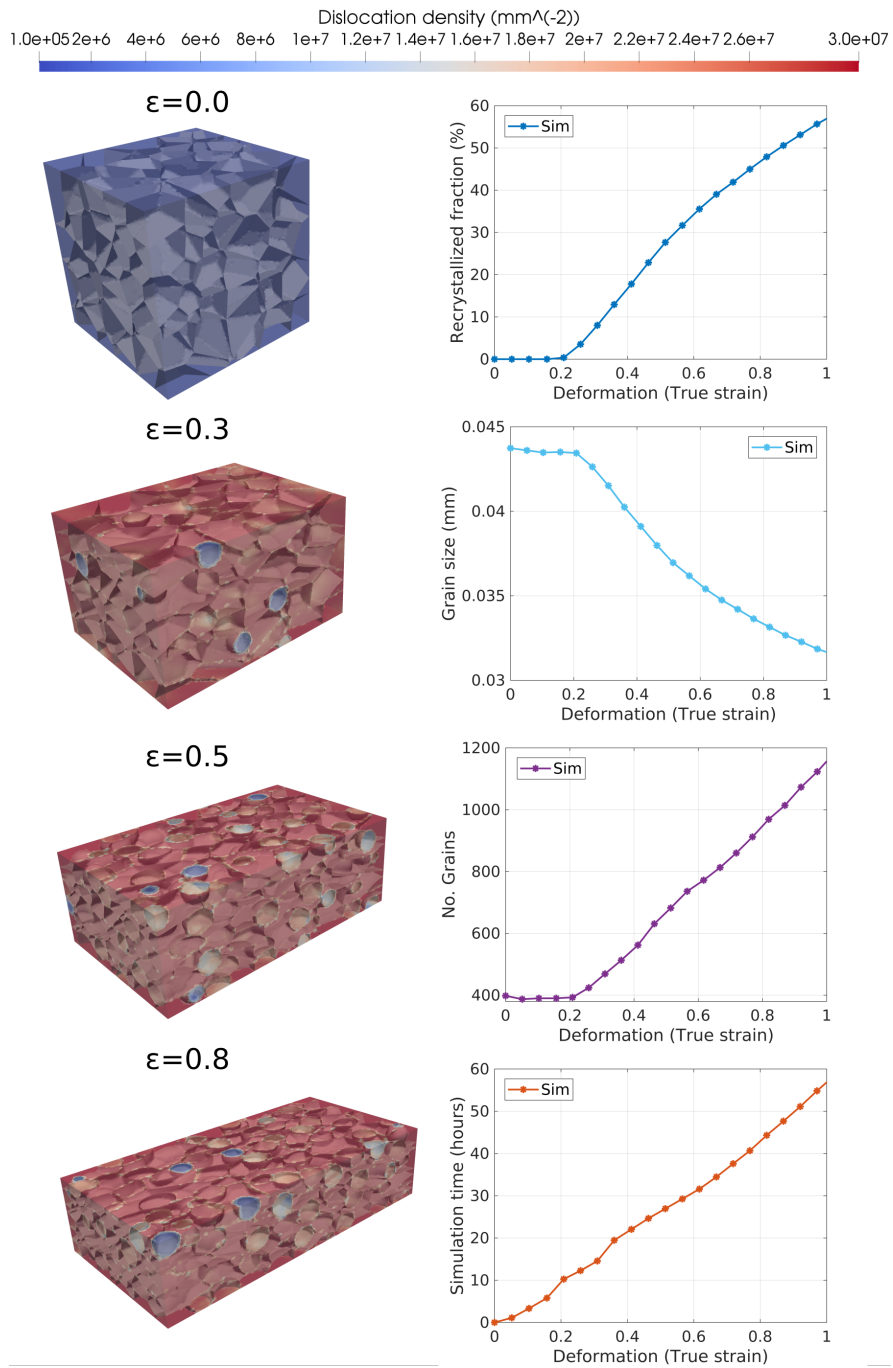


Figure 5: Example simulation of compression of a domain composed of 400 initial grains.

4. Sensitivity analysis and model results

A sensitivity analysis was performed of the numerical parameters of the model in order to ensure the convergence of the results and minimize the computational cost of the simulations. To perform this study several simulations were performed by changing different numerical parameters according to the studied cases.

The boundary conditions imposed for the simulations represent a channel die compression at a constant strain rate of $0.01(s^{-1})$. Figure 6 shows the schematic of the boundary conditions, the imposed velocity is calculated for the shown faces as the points coordinates multiplied by the strain rate. The remaining Faces are forced to remain flat by imposing a velocity equal to 0, in the direction normal to the face.

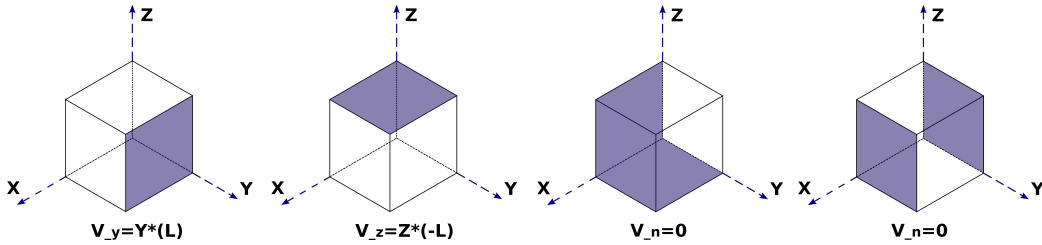


Figure 6: Schematic of the imposed boundary conditions.

The material parameters for the simulations were obtained from [10]. The grains orientation follows a random distribution for all the cases presented in this work. The sensitivity analysis were performed for the different models separately and the coupled model. The analysis were performed in terms of average polycrystal response.

The meshing and remeshing schemes create an isotropic mesh with uniform size. The mesh size is calculated as a function of the nucleus size. As dislocation density increases (due to strain increase) the nuclei size is reduced, causing the mesh to be refined as shown in figure 7.

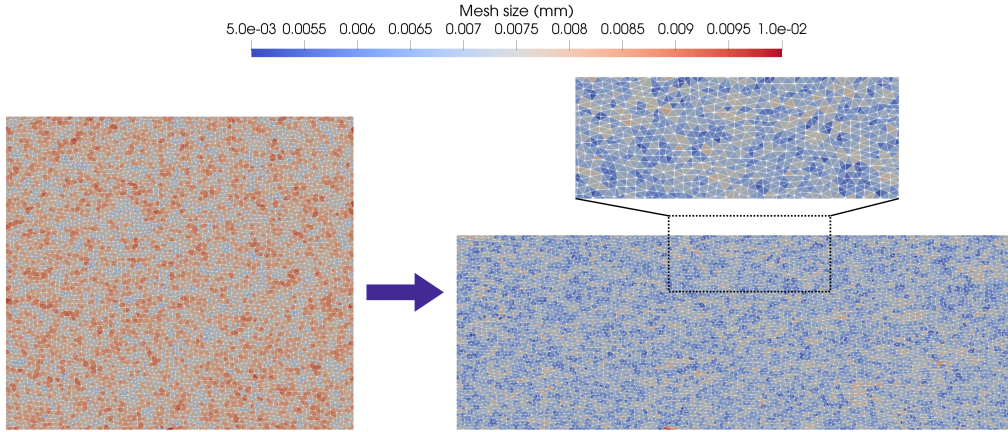


Figure 7: 2D view of the meshing and remeshing scheme after channel die deformation simulation.

4.1. CPFEM

4.1.1. CPFEM model validation

The CPFEM model can be studied both in terms of full FE calculations and also as material point (MP) calculations with only the single crystal model. The CPFEM model developed for this work, was validated both as material point (Taylor model) simulations and as FEM simulations.

For the MP simulations, the cases presented by Marin [54] were reproduced. The simulations consist of the deformation of an aggregate of 256 FCC crystals subjected to plane strain compression and to simple shear. The results are presented in terms macroscopic of stress response and $\langle 111 \rangle$ pole figures before deformation and after deformation. Figure 8 shows the results for both cases.

The results are consistent with the results presented by Marin [54]. The results show that the implemented CP model correctly predicts stress-strain response and texture evolution.

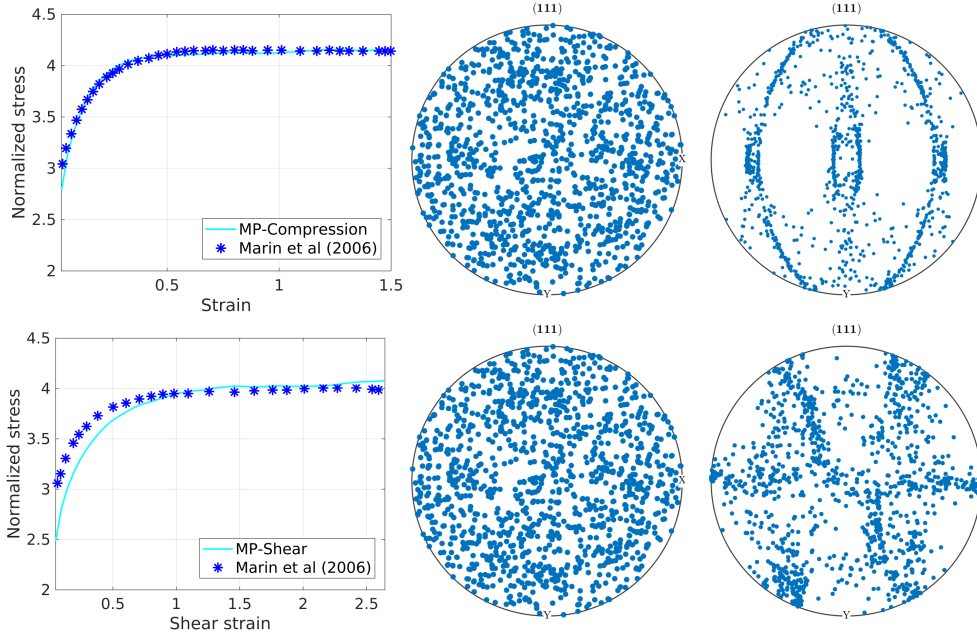


Figure 8: MP simulations of the deformation of an aggregate of 256 FCC crystals subjected to plane strain compression (top side) and to simple shear (bottom side). Macroscopic stress response (left side) and $\langle 111 \rangle$ pole figures before deformation (center) and after deformation (right side). The data from Marin [54] was obtained by digitalizing the published data.

For the FEM simulation, the deformation of 304L steel presented by Fabiano [64] was reproduced. The simulations consist of a channel die compression of a $0.5 \times 0.5 \times 0.5 \text{ mm}$ – 100 grains polycrystal. The results are presented in terms of average stress response and average dislocation density. Figure 9 shows the simulation results.

The results are consistent with the experimental measurements and the simulation results presented by Fabiano [64]. The results show that the CPFEM model correctly predicts the experimental average stress-strain response, and the dislocation density evolution agrees with literature simulations results, in terms of average response and local distribution.

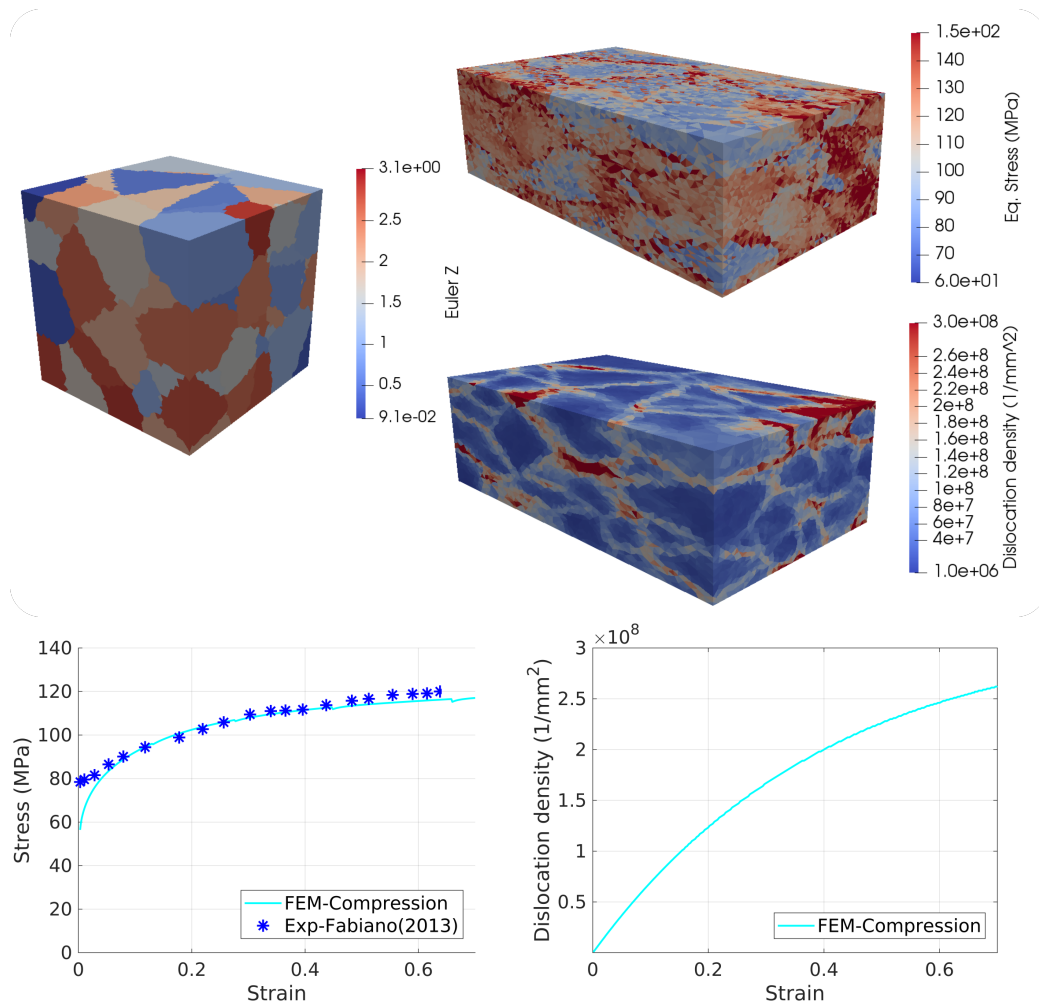


Figure 9: Channel die compression, in terms of average stress and average dislocation density, of a 304L $0.5 \times 0.5 \times 0.5 \text{ mm}$ – 100 grains polycrystal. The experimental data from Fabiano [64] was obtained by digitalizing the published data.

4.1.2. CPFEM mesh size

For the CPFEM calculation the number of elements required to ensure convergence in the solution was studied. The analysis is performed in terms of number of elements per grain, calculated as the average equivalent grain diameter divided by the average mesh size.

For this analysis, CPFEM simulations on a domain of 200 grains, with a grain average size of 0.05 mm , with different mesh sizes were performed. The

simulations were performed up to a deformation of 25% without remeshing operations. The mesh size range considered was from 4.0 up to 8.0 elements per grain. The lower value of 4.0 elements per grain corresponds to the minimum value defined by Maire et al. [25], as the number of elements required to ensure a correct representation of the nuclei topology. The results in terms of average response are presented in figure 10.

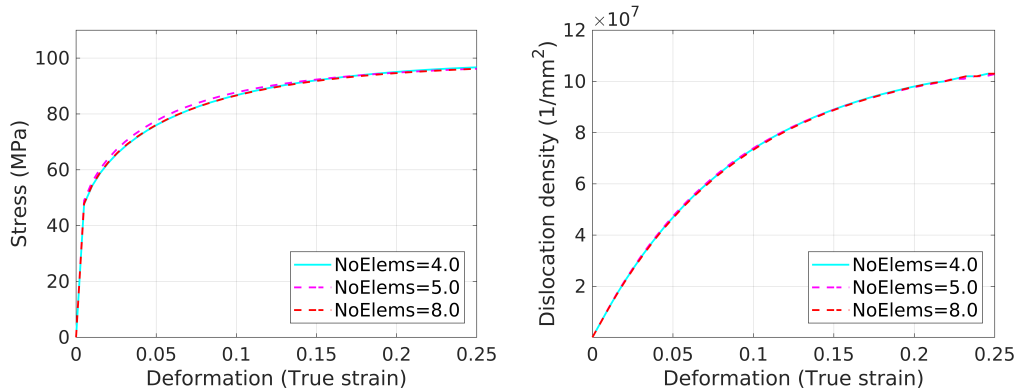


Figure 10: Stress vs strain curve (left side) and dislocation density vs strain curve (right side) for CPFEM simulations for different number of elements per grain. For a domain of 200 grains, with a grain average size of 0.05 mm.

The results showed that 4 elements per grain radius ensure a good average response in terms of convergence for the CPFEM simulations.

To check the convergence in terms of local evolution, simulations of the deformation of a polycrystal with different mesh sizes were compared. To perform the comparison, the same sites were used in the Voronoi tessellation algorithm used to generate the microstructures, and the same initial orientations and dislocation density were assigned to each grain. The local dislocation density distribution weighted by the volume of the elements at different deformation levels, for the considered mesh sizes, are shown in figure 11. The mean L^2 difference (calculated by interpolating results of each simulation to a common mesh, Eq. 29) with respect to the case with the smaller mesh size were also calculated and are shown in figure 12.

$$L^2 = 100 * \sqrt{\frac{\sum_{i=1}^N (v_i - v'_i)^2}{\sum_{i=1}^N (v'_i)^2}}, \quad (29)$$

with N the number of elements, v_i the variable value in the element i and v'_i the reference variable value in the element i .

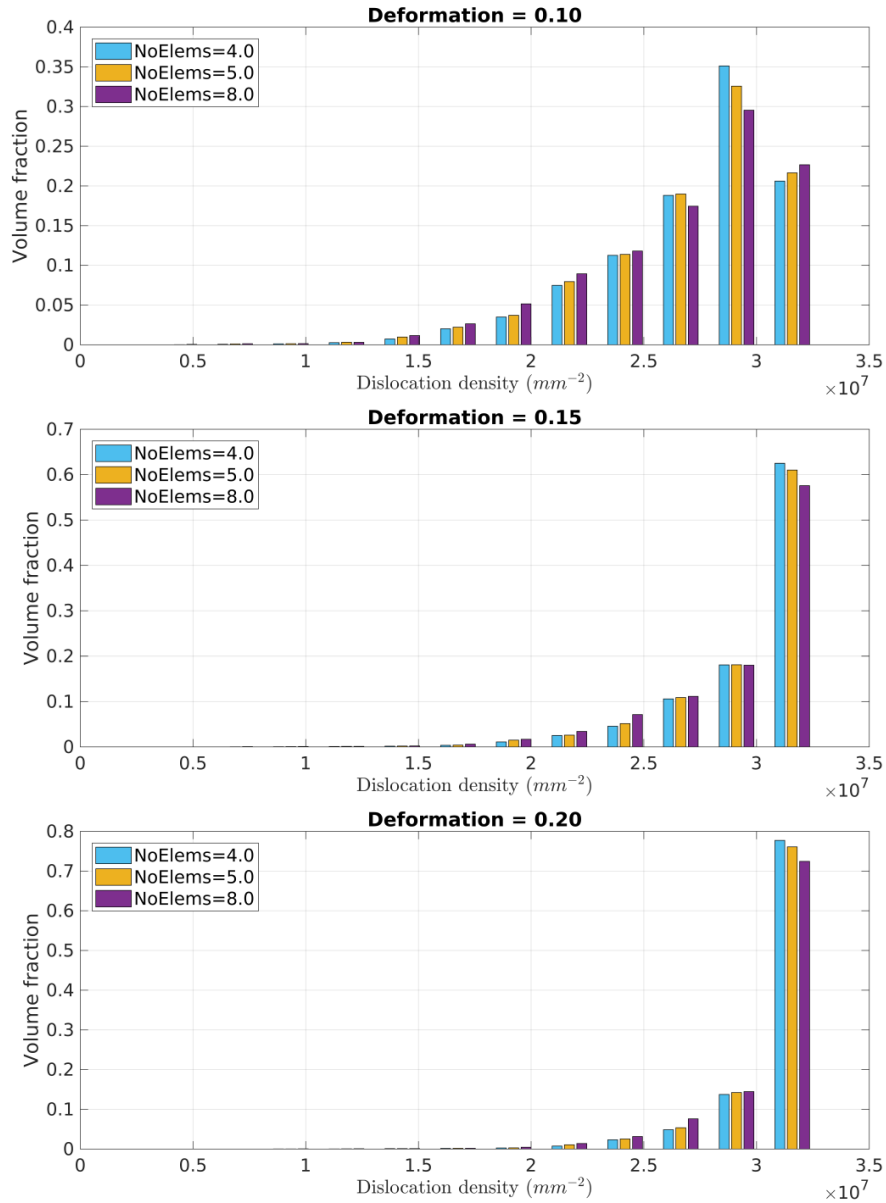


Figure 11: Comparison of the local dislocation density distribution in volume for the simulations of an identical polycrystal with different mesh sizes, for different deformation levels ($\epsilon = 0.10$ top, $\epsilon = 0.15$ middle, $\epsilon = 0.20$ bottom).

The results show moderate differences at that at the local level for the different mesh sizes. Bigger mesh sizes give a more stiff response of the polycrystal. With the increase in deformation more elements reach the maximum dislocation density, behaviour determined by the used hardening law. This reduces the heterogeneity in the field and causes a reduction in the differences between the different mesh sizes. Since the reduction in the mesh size causes a significant increase in the computational cost, the choice in the mesh size will finally be a compromise between the required accuracy and the available computational resources. Here the value of four elements per grain radius will be used as the minimal value for the CPFEM simulations in which the average response is analyzed. For the DRX simulations the mesh size required for the grain boundary migration calculation, the mesh size required for correct representation of the nuclei, and the domain size i.e. number of grains, also need to be considered. This is presented in the following sections.

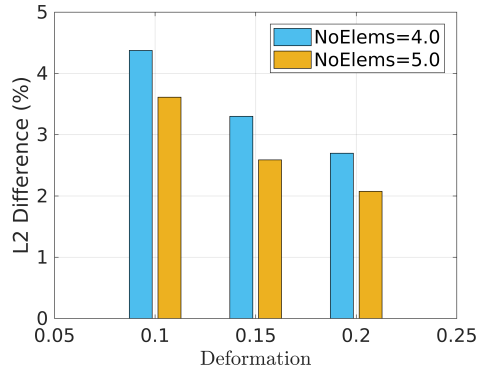


Figure 12: Mean L2 differences of the local dislocation density for the simulations of an identical polycrystal with different mesh sizes, calculated with respect to the case with the smaller mesh size, for different deformation levels.

4.1.3. Number of grains

The number of grains in the domain required to obtain convergence in the response was analyzed. For this, simulations were performed for different domains size i.e. different number grains, with an average grain size of 0.05 mm. Figure 13 shows the responses in terms of stress and dislocation density.

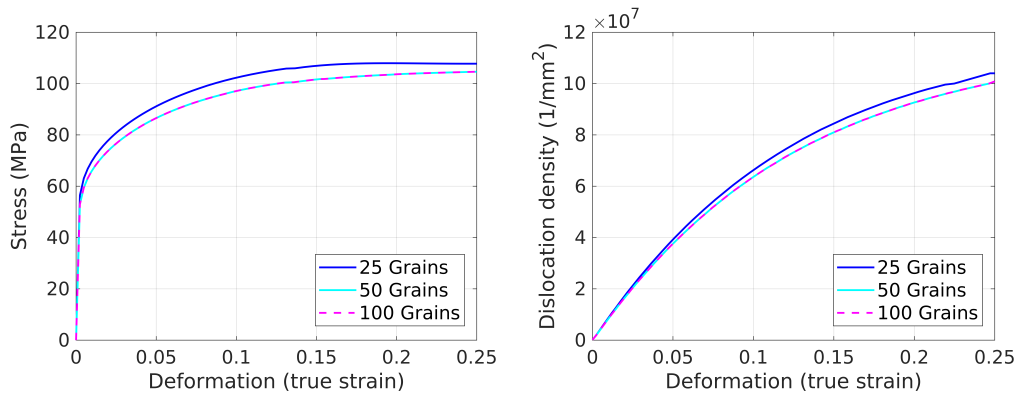


Figure 13: Stress vs strain (left side) and dislocation density vs strain (right side) response for simulations with different initial number of grains.

The results showed that 50 grains ensure convergence in the polycrystal response. Lower number of grains causes that the average polycrystal response depends on the orientations assigned to the initial microstructure.

4.1.4. Deformation step

The final parameter studied was the deformation step (time step). Since CP is a highly non-linear problem, choosing an adequate mesoscale deformation step is very important to ensure the convergence of the computation.

However the non-linearity of the problem changes as the material evolves. Being the elasto-plastic transition (initial part of the stress-strain curve) the more complex to resolve, followed by the plastic-hardening part (the material hardens as it is deformed), and finally the saturation part (material no longer hardens) being the less complex to resolve.

Additionally when coupled with the GBM migration and nucleation models, the movement of the grains boundaries and the appearance of new grains introduce localized gradients, that make the following calculation more complex to resolve.

Because of the previous considerations a very small deformation step is required in order to ensure converge during all the states of the simulation. However keeping a very small deformation step during all simulation increases drastically the total computational time.

The best alternative in order to ensure convergence and minimize the computational cost, is to dynamically calculate the deformation step during the deformation. The criteria used to calculate the deformation step, is based

on the number of iterations required by the non-linear FE solver, to reach convergence at each time step.

An optimal interval for the number of iterations, in terms of computational cost, was identified. If the number of iterations is larger than the max identified value, the time step is reduced by half for the next iteration. If convergence is not reached the time step is reduced by half and the calculation is performed again. If the number of iterations is lower than the minimal identified value the time step is multiplied by a factor of 1.5.

Figure 14 shows the stress vs strain curve and the deformation step vs strain curve, for a CPFEM simulation. This result illustrates that the optimal deformation step varies between 0.1% and 1%, and the optimal deformation time step changes according to the material evolution.

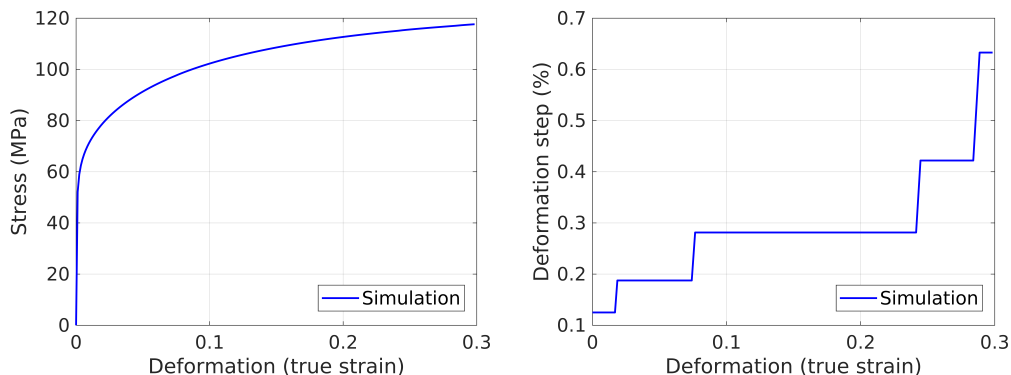


Figure 14: Stress vs strain curve (left side) and Deformation step vs strain curve (right side) for CP simulation of 304L steel at a constant strain rate of $0.01s^{-1}$.

4.2. GBM

In the previous section the numerical parameters for the CPFEM calculation were analyzed. Since the GBM requires the FE solution of a different equation, the numerical parameters for the GBM calculation must also be analyzed. The parameters analyzed were time step and the mesh size relative to the grain size. Simulations of the GBM of a single spherical grain, immersed in an homogeneous matrix were performed. The grain dislocation density was initialized to ρ_0 and the matrix was initialized to the maximum dislocation density defined by $K1/K2$. Additionally the grain dislocation density was evolved following the YLJ hardening equation for a constant macroscopic strain rate of $0.01(s^{-1})$.

The results were compared with the analytical solution available in [25]. Figure 15 shows the error of the simulated GBM in terms of calculated grain size for different mesh sizes and time steps, with respect to the analytical solution for the grain size. The mesh sizes analyzed were defined by considering the minimal number of elements required to correctly describe a spherical grain topology according to [25], and the computational cost related to reducing the mesh size.

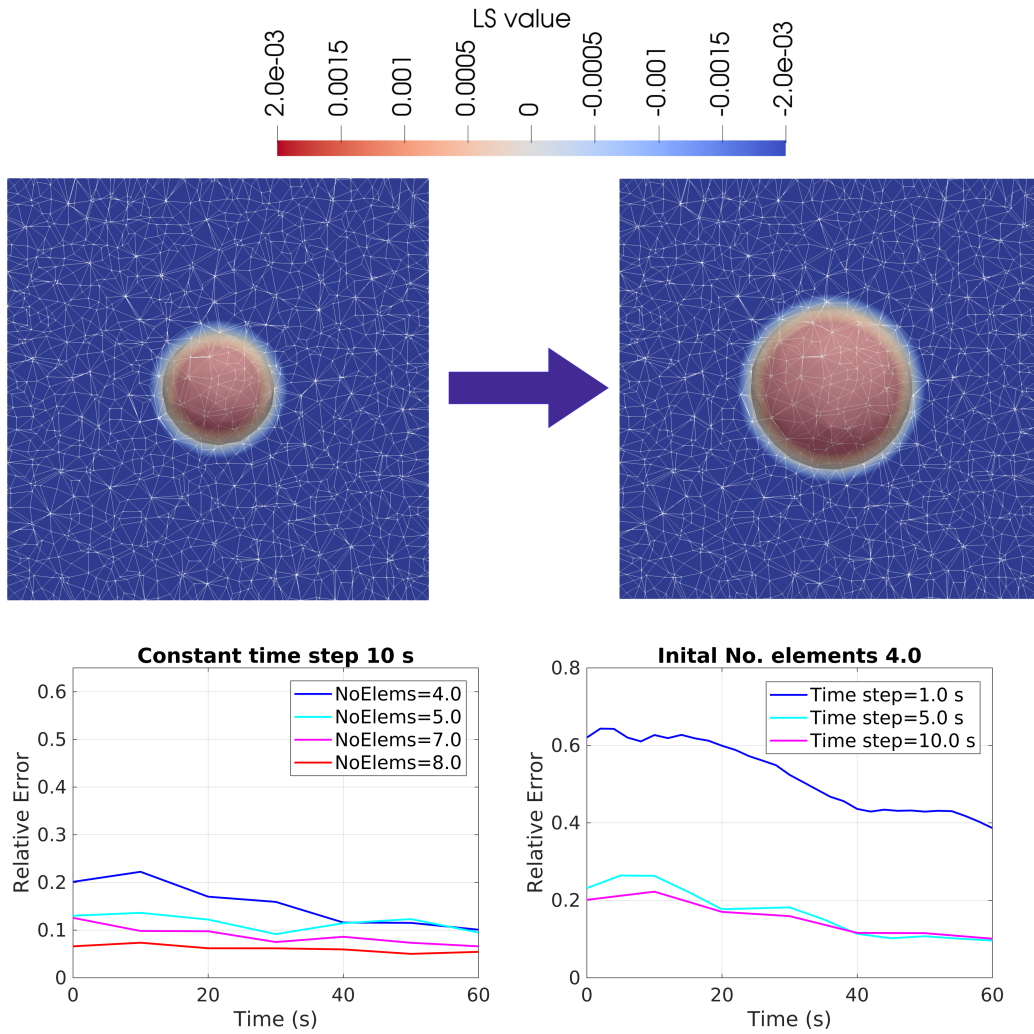


Figure 15: Error of the simulated GBM in terms of grain size for different mesh sizes (left side) and time steps (right side), compared against analytical solution.

The results show that the error is reduced with the decrease in the mesh size, with 8 elements per grain radius showing errors lower than 5%, which is an adequate value for the calculation, considering the increase in computational cost with smaller mesh sizes.

To analyze the error related to the time step it is necessary to consider that the total error in the calculation has multiple sources. Part of the error comes from the temporal discretization and part comes from the resolution methodology. The error related to the discretization can be reduced by refining the time step. The error related to the numerical methodology comes from the numerical operations performed.

The solution of the GBM with the current LS-FE framework requires the performance of several complementary numerical operations (removal of vacuum regions, transport of and reinitialization of the LS function). Each numerical operation introduces errors that accumulate over several iterations. The magnitudes of the introduced numerical errors are related to interpolation of the zero iso-value that defines the GB. Further details of this errors are precisely described and discussed in [65].

One alternative to reduce this errors is to use fitted meshes with nodes located along the zero iso-value of the LS functions. This alternative requires constant remeshing operations that in 3D have currently a prohibitive computational cost. It is not viable option in this work.

Another alternative is the homogeneous reduction of the mesh size to improve the interpolation of the zero iso-value of the LS functions. However this also implies a significant increase of the computational cost.

Finally the alternative used in this work is to minimize the number of operations performed, and to ensure that the magnitude of the calculated displacement of the GB is significantly higher than the introduced numerical errors. This is done by defining an adequate time step for the GBM calculations.

The optimal time step is defined as a compromise that seeks to minimize the errors introduced by the discretization and does not introduce significant error due to the numerical operations.

The results show very similar behavior for the time steps values of 5 and 10 but higher errors for smaller time steps. For this work the range between 5 and 10 s will be chosen for the GBM calculation time step, which is translated in terms of a deformation step.

4.3. Coupled model

Simulations were run to check the number of initial grains required to correctly describe the general behavior of the polycrystal. The results were analyzed in terms of X and \bar{R} . Simulations of the coupled model with different domains sizes, ranging from 20 to 200 initial grains, were run. The results are shown in figure 16.

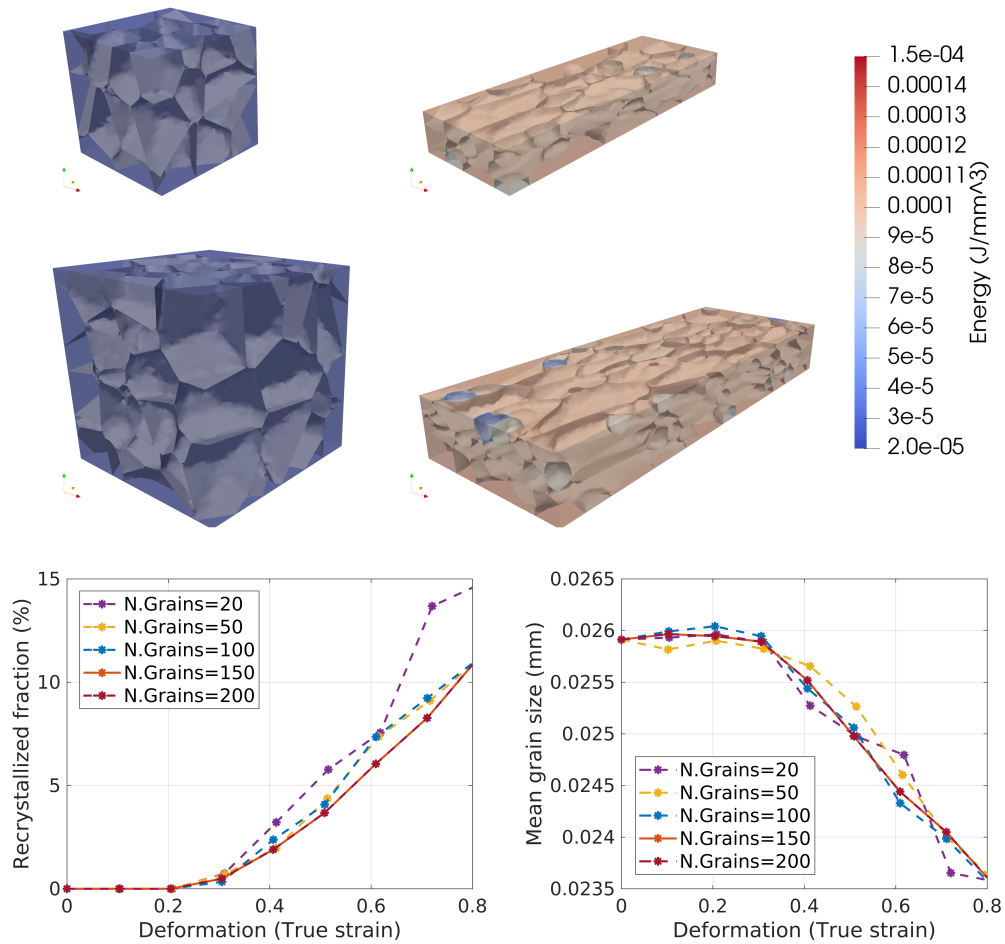


Figure 16: Results of simulations of dynamic recrystallization with different domains sizes, ranging from 20 to 100 initial grains, in terms of X (left) and \bar{R} (right) .

The results show that the minimal number of grains required to ensure

convergence in the simulation results in terms of both X and \bar{R} is 150 grains. Simulations with lower number of grains, 50 and 100, are able to reproduce the same trend, but the results do not show a smooth behaviour. Simulations with lower number of initial grains, 25 grains, show divergence in the results at higher strain levels in terms of X , and more discontinuous behaviour in terms of \bar{R} .

4.4. Nucleation

Since the safety factor w is a purely numerical parameter, it was necessary to analyze its effect on the model results. Simulations with the complete coupled model for a small domain, 10 grains, were performed for different values of w . The grains dislocation density was initialized to a value close to the ρ_{cr} in order to accelerate the appearance of nuclei. A small domain was chosen in order to illustrate more clearly the effect of the nucleated grains in the general behaviour of the microstructure. Figure 17 illustrates the evolution the nucleated grains.

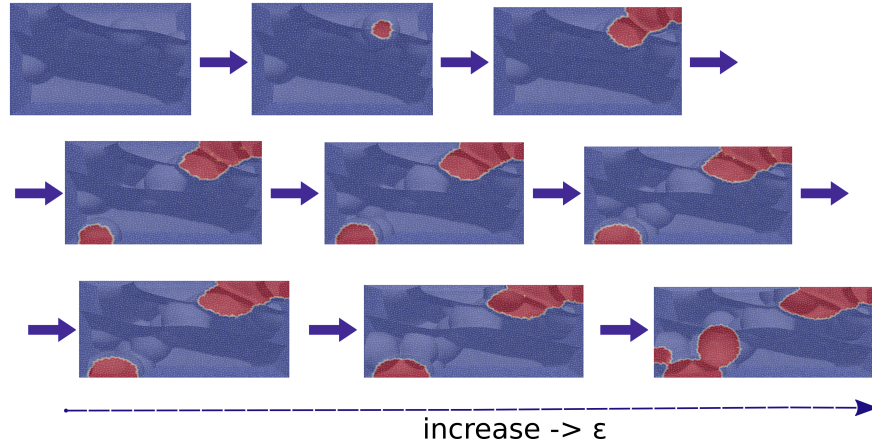


Figure 17: 2D view of the evolution of nucleated grains during DRX simulation of small domain composed of 10 initial grains.

The results are presented in figure 18 in terms of \bar{R} \bar{R}_X . The results show that the value of w has significant effects on the simulation results and leads to over estimations \bar{R} and \bar{R}_X . However Since w modifies the nucleus size, which is used to calculate the mesh size, it also has a very important effect on computational cost of the simulation.

The results also show that if the mesh is sufficient small to correctly describe the nuclei topology it is not necessary to play with the parameter w . So the inclusion of the parameter w in simulations constitutes a choice related to the available computational resources and the required accuracy of the results but must be used carefully.

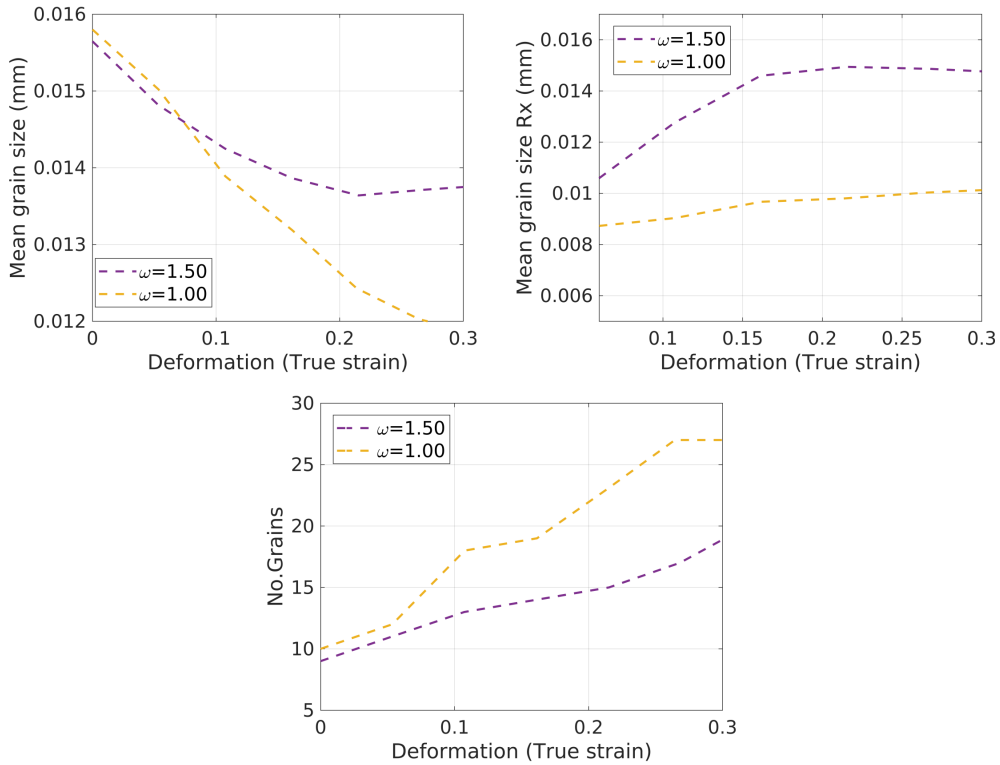


Figure 18: Results of simulations with different w values of 10 grains initialized with a dislocation density value close to ρ_{cr} .

4.5. Nucleus Position

The criteria used to define the nuclei position, which restricts nuclei appearance to only near the grain boundaries, is valid for necklace type nucleation but does not correctly describe other nucleation types. Additional information provided by the CP model can be used to define different criteria for the nuclei position.

To define additional criteria for the nuclei position and test their influence on the simulation results, several simulations were run, each considering

different parameters to define the nuclei position. The different criteria are based on the ρ , orientations are not considered since at the polycrystal scale here, the formation of sub-grain boundaries can not be correctly predicted.

All the criteria tested consider that the dislocation density must reach ρ_{cr} for appearance of a nucleus, to ensure that it will growth. In addition the following criteria were used: First case, nuclei can only appear near the boundary (necklace nucleation considered as a reference simulation). Second case, nuclei can appear anywhere on the domain. Third case, nuclei appear on sites with the highest value of ρ in the domain. Fourth case, nuclei appear on sites with highest ρ gradient. The third and fourth case use the ρ field without averaging it over grains.

The simulations considered a domain of 150 initial grains up to $\epsilon = 1.0$. The results are shown in: figure 19 in terms of X , \bar{R} and \bar{R}_X . Figure 20 in terms of number of neighbours and recrystallized grains number of neighbours. Additionally figure 21 shows the nucleated grains positions at the end of the simulation.

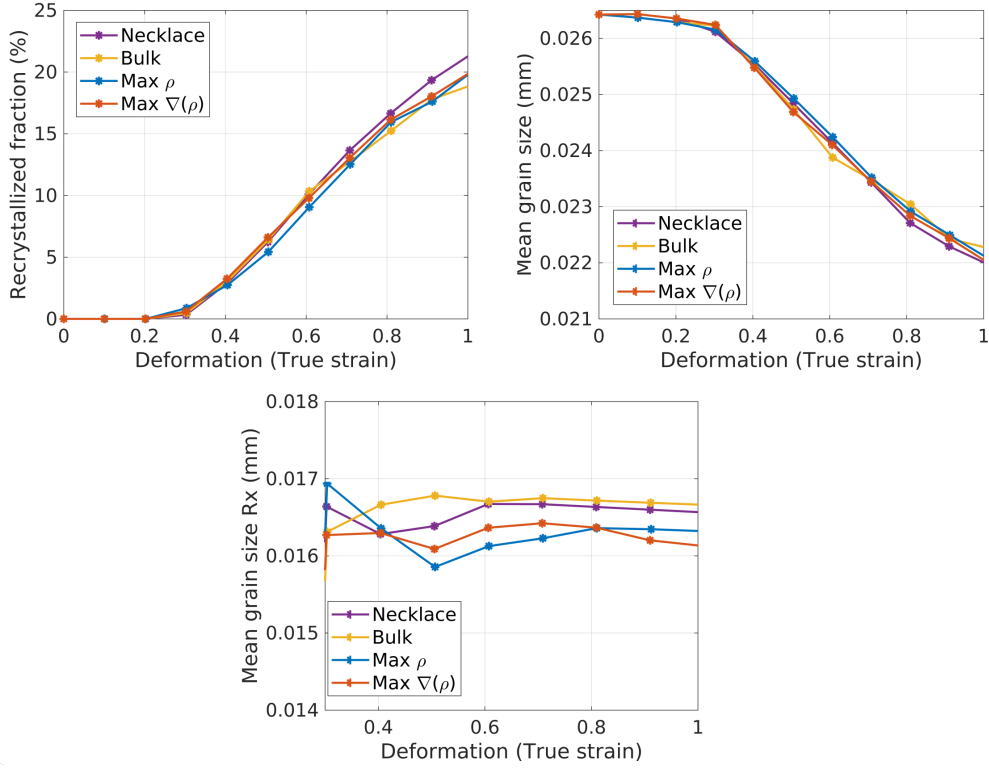


Figure 19: Results of simulations with different criteria for nuclei position, in terms of X , \bar{R} and \bar{R}_X .

The results shows that all cases exhibit very similar behaviour in terms of of X , \bar{R} and number of neighbours. However different behaviours can be seen in terms of \bar{R}_X and recrystallized grains number of neighbours. For deformation lowers than 0.6 the number of nucleus introduced is relatively small, causing more rapid changes in the results.

For the second case, when the deformation is lower than 0.6 the recrystallized grains growth more than all the other cases, since nuclei can appear in the interior of grains, their growth is not limited by others grains, that might have lower energy. With the deformation increasing, most of the grains in the domain reach ρ_{cr} , the behaviour becomes equivalent to that of the reference case. In terms of number of neighbours since the nuclei have more places to appear, less clusters form, so the nuclei have a lower number of neighbours.

For the third case, the nuclei show lower sizes during all the simulation. Local max ρ values appear first near multiple grain boundaries and near

the domain boundaries, since the highest deformation incompatibilities are located in these positions. This causes that nuclei tend be near grains with lower ρ values than the grain they appear on, which limits their growth. In terms of neighbours they show lowest number of neighbours of all the cases during all the simulation. At high deformation when most of the domain has reached the max ρ value, less localized max values are found so the behaviour becomes similar to case 2.

The fourth case shows the highest clustering of nuclei, with the highest number of neighbours during all the simulation, condition that also causes that clustered nucleus limit each other growth. This behaviour is the result of the reinitialization of ρ to ρ_0 when a nucleus is introduced, which creates very high gradients of ρ .

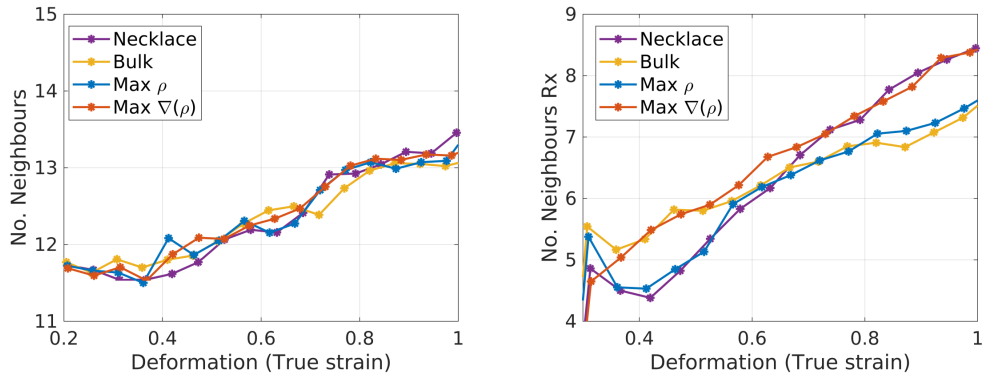


Figure 20: Results of simulations with different criteria for nuclei position, in terms of grains number of neighbours and recrystallized grains number of neighbours.

The overall test showed that in all cases the general microstructural behaviour, remains the same, so each could be used in theory to simulate the behaviour of the polycrystal. It is necessary to compare the simulations results with experimental data in order to define which criteria fits better the actual physical phenomena. Additionally the criteria can be modified by defining limit values instead of just max values.

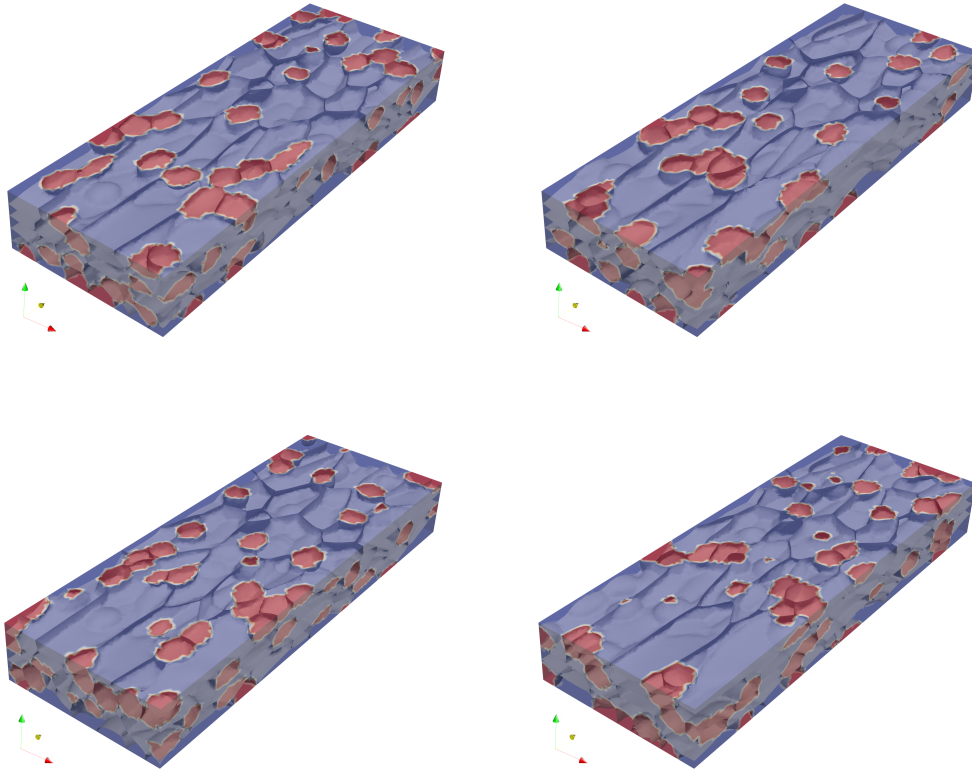


Figure 21: Recrystallized grains of simulations with different criteria for nucleus position. Top left case 1, top right case 2, bottom left case 3 and bottom right case 4. Red color corresponds to the recrystallized grains.

5. Conclusions

In the present work a CPFEM model was coupled with a LS-FE formulation for GBM and phenomenological laws, in order to perform 3D full field simulations of dynamic recrystallization up to high deformation in metals. The inclusion of the CPFEM model allows a much better representation of the plastic deformation phenomena than previous phenomenological approaches [25].

The inclusion of CPFEM model, not only represents a better description of the plastic deformation phenomena, but also since during dynamic recrystallization several processes interact with each other, it provides more accurate input information for the additional models.

The coupled model is able to account for the major physical phenomena happening during dynamic recrystallization and constitutes an interesting numerical framework to perform further improvements.

The results of the implemented CP were compared with results of models and experimental measurements from the literature [54, 64]. The model results showed very good agreement with the models from the literature and with pre-existing experimental measurements.

A coupling algorithm was developed, that minimizes the computational cost, which is one of the main limitations of the CP model, while ensuring the accuracy and correct behavior of all the models.

The models numerical parameters were analyzed, keeping into account the interactions of the different models. Values that ensure convergence of the results and minimize the computational cost were found.

The additional information provided by the crystal plasticity model was also used to define different criteria for the position of nucleus, and the effect on the simulations results were compared for an austenitic stainless steel.

The next step of this work will be the validation of the model results thanks to detailed experimental data.

Data availability

The raw data required to reproduce these findings cannot be shared at this time as the data also forms part of an ongoing study. The processed data required to reproduce these findings cannot be shared at this time as the data also forms part of an ongoing study.

CRedit author statement

- D. A. Ruiz Sarrazola: Conceptualization, Methodology, Software, Formal analysis, Data curation, Writing - original draft.
- D. Pino Muñoz: Conceptualization, Software, Validation, Writing - review & editing, Visualization, Supervision.
- M. Bernacki: Conceptualization, Software, Validation, Writing - review & editing, Visualization, Supervision, Project administration.

Declaration of interest

The authors declare that they have no known competing financial interests or personal relationships that could have appeared to influence the work reported in this paper.

Acknowledgments

The authors thank the ArcelorMittal, ASCOMETAL, AUBERT & DUVAL, CEA, FRAMATOME, SAFRAN, TIMET, Constellium and TRANSVALOR companies and the ANR for their financial support through the DIGIMU consortium and ANR industrial Chair.

Appendix A. Animations

Animation 1: Example of the dislocation density evolution in a full field simulation of DDRX of 304L steel up to $\epsilon = 1.0$. The initial simulation domain composed is composed 400 grains.

References

- [1] A. D. Rollett, G. S. Rohrer, F. J. Humphreys, Recrystallization and related annealing phenomena., 3rd ed., Elsevier, 2017.
- [2] K. Huang, R. E. Logé, A review of dynamic recrystallization phenomena in metallic materials, *Mater. Des.* 111 (2016) 548–574. doi:10.1016/j.matdes.2016.09.012.
- [3] L. Madej, M. Sitko, M. Pietrzyk, Perceptive comparison of mean and full field dynamic recrystallization models, *Arch. Civ. Mech. Eng.* 16 (2016) 569–589. doi:10.1016/j.acme.2016.03.010.
- [4] T. O. Saetre, O. Hunderi, E. Nes, Computer simulation of primary recrystallisation microstructures: The effects of nucleation and growth kinetics, *Acta Metall.* 34 (1986) 981–987. doi:10.1016/0001-6160(86)90207-5.
- [5] K. Marthinsen, O. Lohne, E. Nes, The development of recrystallization microstructures studied experimentally and by computer simulation, *Acta Metall.* 37 (1989) 135–145. doi:10.1016/0001-6160(89)90273-3.
- [6] T. Furu, K. Marthinsen, E. Nes, Modelling recrystallisation, *Mater. Sci. Technol. (United Kingdom)* 6 (1990) 1093–1102. doi:10.1179/mst.1990.6.11.1093.

- [7] O. Beltran, K. Huang, R. Logé, R. Loge, A mean field model of dynamic and post-dynamic recrystallization predicting kinetics, grain size and flow stress, *Comput. Mater. Sci.* 102 (2015) 293–303. doi:10.1016/J.COMMATSCI.2015.02.043.
- [8] P. Bernard, S. Bag, K. Huang, R. Loge, A two-site mean field model of discontinuous dynamic recrystallization, *Mater. Sci. Eng. A* 528 (2011) 7357–7367. doi:10.1016/J.MSEA.2011.06.023.
- [9] D. G. Cram, H. S. Zurob, Y. J. Brechet, C. R. Hutchinson, Modelling discontinuous dynamic recrystallization using a physically based model for nucleation, *Acta Mater.* 57 (2009) 5218–5228. doi:10.1016/j.actamat.2009.07.024.
- [10] L. Maire, Full field and mean field modeling of dynamic and post-dynamic recrystallization in 3D. Application to 304L steel, Ph.D. thesis, MINES ParisTech, 2018.
- [11] F. Montheillet, O. Lurdos, G. Damamme, A grain scale approach for modeling steady-state discontinuous dynamic recrystallization, *Acta Mater.* 57 (2009) 1602–1612. doi:10.1016/j.actamat.2008.11.044.
- [12] M. Zouari, N. Bozzolo, R. E. Loge, Mean field modelling of dynamic and post-dynamic recrystallization during hot deformation of Inconel 718 in the absence of δ phase particles, *Mater. Sci. Eng. A* 655 (2016) 408–424. doi:10.1016/j.msea.2015.12.102.
- [13] M. S. Chen, W. Q. Yuan, H. B. Li, Z. H. Zou, Modeling and simulation of dynamic recrystallization behaviors of magnesium alloy AZ31B using cellular automaton method, *Comput. Mater. Sci.* 136 (2017) 163–172. doi:10.1016/j.commatsci.2017.05.009.
- [14] X. Li, X. Li, H. Zhou, X. Zhou, F. Li, Q. Liu, Simulation of dynamic recrystallization in AZ80 magnesium alloy using cellular automaton, *Comput. Mater. Sci.* 140 (2017) 95–104. doi:10.1016/j.commatsci.2017.08.039.
- [15] D. Raabe, Introduction of a scalable three-dimensional cellular automaton with a probabilistic switching rule for the discrete mesoscale simulation of recrystallization phenomena, *Philos. Mag. A Phys.*

- Condens. Matter, Struct. Defects Mech. Prop. 79 (1999) 2339–2358. doi:10.1080/01418619908214288.
- [16] A. D. Rollett, D. J. Srolovitz, M. P. Anderson, Simulation and theory of abnormal grain growth-anisotropic grain boundary energies and mobilities, *Acta Metall.* 37 (1989) 1227–1240. doi:10.1016/0001-6160(89)90117-X.
- [17] A. D. Rollett, D. Raabe, A hybrid model for mesoscopic simulation of recrystallization, *Comput. Mater. Sci.* 21 (2001) 69–78. doi:10.1016/S0927-0256(00)00216-0.
- [18] H. Zhang, J. Wang, Q. Chen, D. Shu, C. Wang, G. Chen, Z. Zhao, Study of dynamic recrystallization behavior of T2 copper in hot working conditions by experiments and cellular automaton method, *J. Alloys Compd.* 784 (2019) 1071–1083. URL: <https://doi.org/10.1016/j.jallcom.2019.01.132>. doi:10.1016/j.jallcom.2019.01.132.
- [19] L. A. Barrales Mora, G. Gottstein, L. S. Shvindlerman, Three-dimensional grain growth: Analytical approaches and computer simulations, *Acta Mater.* 56 (2008) 5915–5926. doi:10.1016/j.actamat.2008.08.006.
- [20] J. Lépinoux, D. Weygand, M. Verdier, Modélisation de la croissance de grains par dynamique de vertex, *Comptes Rendus Phys.* 11 (2010) 265–273. doi:10.1016/j.crhy.2010.07.015.
- [21] M. Bernacki, Y. Chastel, T. Coupez, R. Logé, Level set framework for the numerical modelling of primary recrystallization in polycrystalline materials, *Scr. Mater.* 58 (2008) 1129–1132. doi:10.1016/J.SCRIPTAMAT.2008.02.016.
- [22] M. Bernacki, R. E. Logé, T. Coupez, Level set framework for the finite-element modelling of recrystallization and grain growth in polycrystalline materials, *Scr. Mater.* 64 (2011) 525–528. doi:10.1016/J.SCRIPTAMAT.2010.11.032.
- [23] M. Elsey, S. Esedoglu, P. Smereka, Diffusion generated motion for grain growth in two and three dimensions, *J. Comput. Phys.* 228 (2009) 8015–8033. doi:10.1016/j.jcp.2009.07.020.

- [24] H. Hallberg, A modified level set approach to 2D modeling of dynamic recrystallization, *Model. Simul. Mater. Sci. Eng.* 21 (2013). doi:10.1088/0965-0393/21/8/085012.
- [25] L. Maire, B. Scholtes, C. Moussa, N. Bozzolo, D. P. Muñoz, A. Settefrati, M. Bernacki, Modeling of dynamic and post-dynamic recrystallization by coupling a full field approach to phenomenological laws, *Mater. Des.* 133 (2017) 498–519. doi:10.1016/j.matdes.2017.08.015.
- [26] B. Merriman, J. K. Bence, O. S. J., Motion of Multiple Junctions: A Level Set Approach, *J. Comput. Phys.* 112 (1994) 334–363. doi:10.1006/jcph.1994.1105.
- [27] E. Borukhovich, P. S. Engels, J. Mosler, O. Shchyglo, I. Steinbach, Large deformation framework for phase-field simulations at the mesoscale, *Comput. Mater. Sci.* 108 (2015) 367–373. URL: <http://dx.doi.org/10.1016/j.commatsci.2015.06.021>. doi:10.1016/j.commatsci.2015.06.021.
- [28] K. Chang, L. Q. Chen, C. E. Krill, N. Moelans, Effect of strong nonuniformity in grain boundary energy on 3-D grain growth behavior: A phase-field simulation study, *Comput. Mater. Sci.* 127 (2017) 67–77. URL: <http://dx.doi.org/10.1016/j.commatsci.2016.10.027>. doi:10.1016/j.commatsci.2016.10.027.
- [29] R. Darvishi Kamachali, I. Steinbach, 3-D phase-field simulation of grain growth: Topological analysis versus mean-field approximations, *Acta Mater.* 60 (2012) 2719–2728. doi:10.1016/j.actamat.2012.01.037.
- [30] C. Krill III, L.-Q. Chen, Computer simulation of 3D grain growth using a phase field model, *Acta Mater.* 50 (2002) 3059–3075. doi:10.1016/s1359-6454(02)00084-8.
- [31] C. Schwarze, R. Darvishi Kamachali, M. Kühbach, C. Mießen, M. Tegeler, L. Barrales-Mora, I. Steinbach, G. Gottstein, Computationally Efficient Phase-field Simulation Studies Using RVE Sampling and Statistical Analysis, *Comput. Mater. Sci.* 147 (2018) 204–216. doi:10.1016/j.commatsci.2018.02.005.

- [32] I. Steinbach, O. Shchyglo, Phase-field modelling of microstructure evolution in solids: Perspectives and challenges, *Curr. Opin. Solid State Mater. Sci.* 15 (2011) 87–92. doi:10.1016/j.cossms.2011.01.001.
- [33] Y. Jin, N. Bozzolo, A. D. Rollett, M. Bernacki, 2D finite element modeling of misorientation dependent anisotropic grain growth in polycrystalline materials: Level set versus multi-phase-field method, *Comput. Mater. Sci.* (2015). doi:10.1016/j.commatsci.2015.03.012.
- [34] C. Mieben, M. Liesenjohann, L. A. Barrales-Mora, L. S. Shvindlerman, G. Gottstein, An advanced level set approach to grain growth - Accounting for grain boundary anisotropy and finite triple junction mobility, *Acta Mater.* 99 (2015) 39–48. doi:10.1016/j.actamat.2015.07.040.
- [35] B. Scholtes, M. Shakoor, A. Settefrati, P. O. Bouchard, N. Bozzolo, M. Bernacki, New finite element developments for the full field modeling of microstructural evolutions using the level set method, *Comput. Mater. Sci.* 109 (2015) 388–398. doi:10.1016/j.commatsci.2015.07.042.
- [36] M. Shakoor, B. Scholtes, P. O. Bouchard, M. Bernacki, An efficient and parallel level set reinitialization method. Application to micromechanics and microstructural evolutions, *Appl. Math. Model.* 39 (2014) 7291–7302. doi:10.1016/j.apm.2015.03.014.
- [37] A. M. Habraken, Modelling the plastic anisotropy of metals, *Arch. Comput. Methods Eng.* 11 (2004) 3–96. doi:10.1007/BF02736210.
- [38] F. Roters, P. Eisenlohr, L. Hantcherli, D. Tjahjanto, T. Bieler, D. Raabe, Overview of constitutive laws, kinematics, homogenization and multiscale methods in crystal plasticity finite-element modeling: Theory, experiments, applications, *Acta Mater.* 58 (2010) 1152–1211. doi:10.1016/J.ACTAMAT.2009.10.058.
- [39] F. Roters, P. Eisenlohr, T. R. Bieler, D. Raabe, Crystal Plasticity Finite Element Methods: In *Materials Science and Engineering*, 2010. doi:10.1002/9783527631483.
- [40] P. Van Houtte, S. Li, M. Seefeldt, L. Delannay, Deformation texture prediction: from the Taylor model to the advanced Lamel model, *Int. J. Plast.* 21 (2005) 589–624. doi:10.1016/J.IJPLAS.2004.04.011.

- [41] T. Tang, G. Zhou, Z. Li, D. Li, L. Peng, Y. Peng, P. Wu, H. Wang, M. G. Lee, A polycrystal plasticity based thermo-mechanical-dynamic recrystallization coupled modeling method and its application to light weight alloys, *Int. J. Plast.* 116 (2019) 159–191. doi:10.1016/j.ijplas.2019.01.001.
- [42] G. Zhou, Z. Li, D. Li, Y. Peng, H. Wang, P. Wu, Misorientation development in continuous dynamic recrystallization of AZ31B alloy sheet and polycrystal plasticity simulation, *Mater. Sci. Eng. A* 730 (2018) 438–456. doi:10.1016/j.msea.2018.05.095.
- [43] G. Zhou, Z. Li, D. Li, Y. Peng, H. S. Zurob, P. Wu, A polycrystal plasticity based discontinuous dynamic recrystallization simulation method and its application to copper, *Int. J. Plast.* 91 (2017) 48–76. doi:10.1016/j.ijplas.2017.01.001.
- [44] L. Madej, M. Sitko, A. Legwand, K. Perzynski, K. Michalik, Development and evaluation of data transfer protocols in the fully coupled random cellular automata finite element model of dynamic recrystallization, *Journal of Computational Science* 26 (2018) 66–77. doi:10.1016/j.jocs.2018.03.007.
- [45] E. Popova, Y. Staraselski, A. Brahme, R. K. Mishra, K. Inal, Coupled crystal plasticity - Probabilistic cellular automata approach to model dynamic recrystallization in magnesium alloys, *Int. J. Plast.* (2015). doi:10.1016/j.ijplas.2014.04.008.
- [46] B. Radhakrishnan, G. Sarma, H. Weiland, P. Baggethun, Simulations of deformation and recrystallization of single crystals of aluminium containing hard particles, *Model. Simul. Mater. Sci. Eng.* 8 (2000) 737–750. doi:10.1088/0965-0393/8/5/307.
- [47] A. D. Tutcuoglu, A. Vidyasagar, K. Bhattacharya, D. M. Kochmann, Stochastic modeling of discontinuous dynamic recrystallization at finite strains in hcp metals, *J. Mech. Phys. Solids* 122 (2019) 590–612. doi:10.1016/j.jmps.2018.09.032.
- [48] L. Chen, J. Chen, R. A. Lebensohn, Y. Z. Ji, T. W. Heo, S. Bhattacharyya, K. Chang, S. Mathaudhu, Z. K. Liu, L. Q. Chen,

- An integrated fast Fourier transform-based phase-field and crystal plasticity approach to model recrystallization of three dimensional polycrystals, *Comput. Methods Appl. Mech. Eng.* 285 (2015). doi:10.1016/j.cma.2014.12.007.
- [49] P. Zhao, T. Song En Low, Y. Wang, S. R. Niezgoda, An integrated full-field model of concurrent plastic deformation and microstructure evolution: Application to 3D simulation of dynamic recrystallization in polycrystalline copper, *Int. J. Plast.* 80 (2016) 38–55. doi:10.1016/j.ijplas.2015.12.010.
- [50] P. Zhao, Y. Wang, S. R. Niezgoda, Microstructural and micromechanical evolution during dynamic recrystallization, *Int. J. Plast.* 100 (2018) 52–68. doi:10.1016/j.ijplas.2017.09.009.
- [51] R. Asaro, A. Needleman, Overview no. 42 Texture development and strain hardening in rate dependent polycrystals, *Acta Metall.* 33 (1985) 923–953. doi:10.1016/0001-6160(85)90188-9.
- [52] E. Marin, P. Dawson, On modelling the elasto-viscoplastic response of metals using polycrystal plasticity, *Comput. Methods Appl. Mech. Eng.* 165 (1998) 1–21. doi:10.1016/S0045-7825(98)00034-6.
- [53] O. C. Zienkiewicz, R. L. Taylor, D. Fox, *The Finite Element Method for Solid and Structural Mechanics*, seventh ed ed., Butterworth-Heinemann, 2014.
- [54] E. B. Marin, On the formulation of a crystal plasticity model., Technical Report, Sandia National Laboratories (SNL), Albuquerque, NM, and Livermore, CA, 2006. doi:10.2172/890604.
- [55] T. Coupez, H. Dignonnet, R. Ducloux, Parallel meshing and remeshing, *Appl. Math. Model.* 25 (2000) 153–175. doi:10.1016/S0307-904X(00)00045-7.
- [56] H. Resk, L. Delannay, M. Bernacki, T. Coupez, R. Logé, Adaptive mesh refinement and automatic remeshing in crystal plasticity finite element simulations, *Model. Simul. Mater. Sci. Eng.* 17 (2009) 075012. doi:10.1088/0965-0393/17/7/075012.

- [57] H. Resk, Finite element modelling of grain-scale heterogeneities in polycrystalline aggregates, Ph.D. thesis, MINES ParisTech, 2010.
- [58] A. Yoshie, H. Morikawa, Y. Onoe, K. Itoh, Formulation of static recrystallization of austenite in hot rolling process of steel plate, *Transactions of the Iron and Steel Institute of Japan* 27 (1987) 425–431. doi:10.2355/isijinternational1966.27.425.
- [59] B. Scholtes, R. Boulais-Sinou, A. Settefrati, D. Pino Muñoz, I. Poitroult, A. Montouchet, N. Bozzolo, M. Bernacki, 3D level set modeling of static recrystallization considering stored energy fields, *Comput. Mater. Sci.* 122 (2016) 57–71. doi:10.1016/J.COMMATSCI.2016.04.045.
- [60] K. Hitti, P. Laure, T. Coupez, L. Silva, M. Bernacki, Precise generation of complex statistical Representative Volume Elements (RVEs) in a finite element context, *Comput. Mater. Sci.* 61 (2012) 224–238. URL: <http://dx.doi.org/10.1016/j.commatsci.2012.04.011>. doi:10.1016/J.COMMATSCI.2012.04.011.
- [61] D. N. Ilin, N. Bozzolo, T. Toulorge, M. Bernacki, Full field modeling of recrystallization: Effect of intragranular strain gradients on grain boundary shape and kinetics, *Comput. Mater. Sci.* 150 (2018) 149–161. doi:10.1016/j.commatsci.2018.03.063.
- [62] W. Roberts, B. Ahlblom, A nucleation criterion for dynamic recrystallization during hot working, *Acta Metall.* 26 (1978) 801–813. doi:10.1016/0001-6160(78)90030-5.
- [63] P. Peczak, M. J. Luton, The effect of nucleation models on dynamic recrystallization: I. Homogeneous stored energy distribution, volume 68, 1993. doi:10.1080/13642819308215285.
- [64] A. L. Fabiano, Modelling of crystal plasticity and grain boundary migration of 304L steel at the mesoscopic scale, Ph.D. thesis, MINES ParisTech, 2013.
- [65] S. Florez, M. Shakoov, T. Toulorge, M. Bernacki, A new finite element strategy to simulate microstructural evolutions, *Computational Materials Science* 172 (2020). In press.

